Volume 8
Number 28
28 July 2020
Pages 9451–9778

Journal of Materials Chemistry C

Materials for optical, magnetic and electronic devices

rsc.li/materials-c

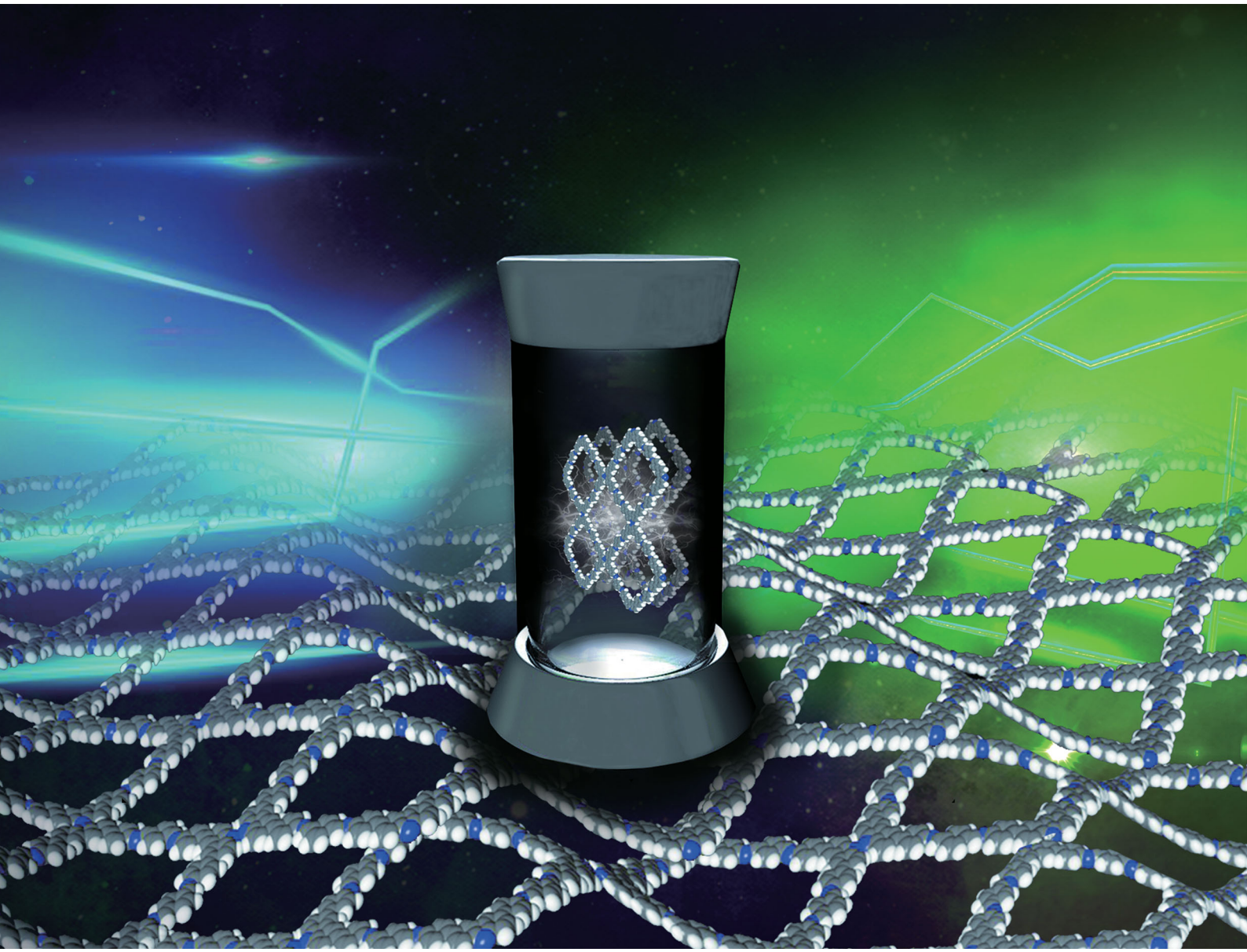

ISSN 2050-7526

ROYAL SOCIETY OF CHEMISTRY

PAPER

Ahmed F. M. EL-Mahdy, Shiao-Wei Kuo *et al.*
A highly fluorescent covalent organic framework as a hydrogen chloride sensor: roles of Schiff base bonding and π-stacking

Journal of Materials Chemistry C

ROYAL SOCIETY OF CHEMISTRY

PAPER

View Article Online
View Journal | View Issue

Cite this: J. Mater. Chem. C, 2020, 8, 9520

A highly fluorescent covalent organic framework as a hydrogen chloride sensor: roles of Schiff base bonding and π-stacking†

Ahmed F. M. EL-Mahdy, *[a] Ming-Yi Lai[a] and Shiao-Wei Kuo *[ab]

In this paper we report the extremely crystalline structures, high thermal stabilities, and strong fluorescence emissions of covalent organic frameworks (COFs) based on linked carbazole units. We have synthesized three stable luminescent carbazole-linked COFs, namely, BCTB–PD, BCTA–TP, and BCTB–BCTA, through Schiff base condensations of 4,4′,4″,4‴-([9,9′-bicarbazole]-3,3′,6,6′-tetrayl)tetrabenzaldehyde (BCTB-4CHO) with *p*-phenylenediamine (PD), of 4,4′,4″,4‴-([9,9′-bicarbazole]-3,3′,6,6′-tetrayl)tetraaniline (BCTA-4NH_2) with terephthalaldehyde (TP), and of BCTB-4CHO with BCTA-4NH_2, respectively. These COFs had large Brunauer–Emmett–Teller surface areas (up to 2212 m^2 g^{-1}) and outstanding thermal stabilities (decomposition temperatures of up to 566 °C). Interestingly, the intramolecular charge transfer (ICT) and fluorescence properties of these COFs were strongly influenced by their types of Schiff base bonding (BCTB-4CH═N or BCTA-4N═CH) and the degrees of π-stacking between their COF layers. For example, ICT from the electron-donating carbazole group to the acceptor through the Schiff base units of the type BCTB-4CH═N and increasing the π-stacking distance enhanced the fluorescence emission from the COF. Moreover, BCTB–BCTA, the most fluorescent of our three COFs, functioned as a fluorescent chemosensor for HCl in solution, with outstanding sensitivity and a rapid response.

Received 16th April 2020,
Accepted 28th May 2020

DOI: 10.1039/d0tc01872d

rsc.li/materials-c

Introduction

Carbazole is an electron-rich tricyclic aromatic heterocyclic compound comprising two benzene rings fused to the sides of a pyrrole ring. Carbazole-based materials are generally highly stable under harsh chemical and environmental conditions. Furthermore, due to their attractive electron-donating and charge-transporting properties, carbazole-based materials have been used in a variety of applications, including energy storage, photoluminescent probes, and organic solar cells (OSCs).[1–10] As an example of energy storage applications, we have recently prepared the carbazole-based covalent organic frameworks (COFs) Car-TPA, Car-TPP, and Car-TPT, containing carbazole units in their hexagonal backbones and exhibiting good specific capacitances (up to 17.4 F g^{-1} at a current density of 0.2 A g^{-1}), through [3+3] and one-pot polycondensations.[5] Moreover, TFP-Car, a β-ketoenamine-tethered COF, obtained through the polycondensation of 1,3,5-triformylphloroglucinol with 9-(4-aminophenyl)carbazole-3,6-diamine, has exhibited a high electrochemical efficiency (up to 149.1 F g^{-1} at a current density of 2 A g^{-1}).[4] In terms of photoluminescence applications, carbazole derivatives have been applied as fluorescent probes for the detection of reactive sulfur, ionic, and oxygen species; the detection of biomacromolecules (*e.g.*, RNA, DNA); and the identification of microenvironments (*e.g.*, pH, viscosity, polarity).[11–18] In OSCs, carbazole-based materials have been used as non-fullerene acceptors (NFAs). For example, carbazole moieties (as core donor units) have been linked with electron-withdrawing groups (as acceptors) to obtain OSCs with power conversion efficiencies (PCEs) of up to 2.56%.[19] In addition, the use of carbazole as a core donor and malononitrile and diketopyrrolopyrrole as terminal units has provided OSCs with PCEs of up to 5.3 and 2.3%, respectively.[20,21] All of these previously reported carbazole-based luminescent materials have been non-crystalline; because as crystalline carbazole-based luminescent materials would presumably possess high surface areas, greater luminescence and extremely high thermal stabilities, their preparation should lead to the development of systems displaying new and attractive properties.

COFs are porous crystalline polymers having two-dimensional (2D) or three-dimensional long-range periodic structures.[22–24] COFs are assembled on the basis of the principle of reticular chemistry, specifically through the cross-linking of organic building blocks through covalent bonds.[25–27] Due to their excellent

[a] Department of Materials and Optoelectronic Science, Center of Crystal Research, National Sun Yat-Sen University, Kaohsiung, 80424, Taiwan. E-mail: ahmed1932005@gmail.com, kuosw@faculty.nsysu.edu.tw
[b] Department of Medicinal and Applied Chemistry, Kaohsiung Medical University, Kaohsiung, 807, Taiwan

† Electronic supplementary information (ESI) available. See DOI: 10.1039/d0tc01872d

crystallinity, permanent porosity, high surface areas, and high thermal stability,[28–31] hundreds of COFs have been synthesized in the past decade with impressive applications in the fields of catalysis, gas adsorption, separation, energy storage, medicine, optoelectronics, proton conduction, and chemical sensing.[4,25,27,32–45] A diverse array of covalent linkages, typically based on B–O, C–C, N–N, C–N, and B–N bonds, have been used to construct COFs with various pore sizes, structures, and functions.[46–49] Although the majority of previously prepared imine-linked COFs have been non-fluorescent or only weakly fluorescent, some highly fluorescent COFs have been constructed recently by using highly emissive building linkers (*e.g.*, pyrene, tetraphenylethylene) or non-emissive building linkers (*e.g.*, hydrazone, hydroquinoline).[50–55] When used as chemosensors, fluorescent COFs have distinct advantages over non-fluorescent ones, due to their more rapid response times, greater sensitivity to changes in their chemical environment, superior physiochemical stability, and monolithic pore sizes.[56] Various fluorescent COFs have been developed recently as chemosensors for mercury ions, pH, 2,4,6-trinitrophenol, electron-rich arenes, iron(III), and anions.[55,57–63] We are, however, aware of only one COF-based sensor for HCl: ETBA-DAB, a COF devolved by Cui *et al.* that functioned as a chemosensor for the sensitive detection of HCl gas.[64] Because the porous crystalline structures of COFs can accommodate gas molecules within their inner channels, there appears to be much room for the development of new COF-based chemosensors.

Although the above examples confirm that it is possible to prepare highly fluorescent COFs, there remains a lack of guiding principles on how to build photoluminescent COFs with enhanced emissive properties. Therefore, in this study, we investigated some of the underlying characteristics affecting the photoluminescence of COFs. We have synthesized three luminescent carbazole-linked COFs, namely, BCTB–PD, BCTA–TP, and BCTB–BCTA, through the reactions of 4,4′,4″,4‴-([9,9′-bicarbazole]-3,3′,6,6′-tetrayl)tetrabenzaldehyde (BCTB-4CHO) with *p*-phenylenediamine (PD), of 4,4′,4″,4‴-([9,9′-bicarbazole]-3,3′,6,6′-tetrayl)tetraaniline (BCTA-4NH_2) with terephthalaldehyde (TP), and of BCTB-4CHO with BCTA-4NH_2, respectively (Scheme 1). We have found that the type of Schiff base bonding units and the degree of π-stacking between the COF layers influenced the fluorescence of these COFs. In addition, BCTB–BCTA COF functioned as a chemosensor for HCl.

Results and discussion

We used Suzuki–Miyaura reactions to synthesize the new precursor tetraaldehyde BCTB-4CHO and the tetraamine BCTA-4NH_2. Briefly, the couplings of 3,3′,6,6′-tetrabromo-9,9′-bicarbazole (BC-4Br) with 4-formylphenylboronic acid and 4-aminophenylboronic acid pinacol ester, performed in 1,4-dioxane/water (1 : 0.2, v/v) in the presence of tetrakis(triphenylphosphine)palladium(0) as the catalyst and K_2CO_3 as the base, resulted in the formation of BCTB-4CHO and BCTA-4NH_2, respectively, in excellent yields. Fourier transform infrared (FTIR) and nuclear magnetic resonance (NMR)

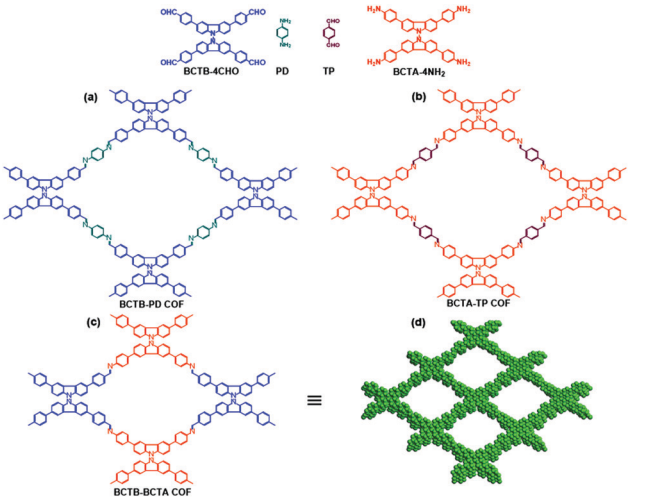

Scheme 1 (a–c) Schematic representation of strategies for the construction of (a) BCTB–PD, (b) BCTA–TP, and (c) BCTB–BCTA COFs; (d) top view of the strongest fluorescent BCTB–BCTA COF, revealing the A–A stacking model.

spectroscopy confirmed the chemical structures of these precursors (Fig. S1–S12, ESI†). The FTIR spectrum of BCTB-4CHO featured adsorption bands at 2803–2717, 1685, and 1589 cm^{-1} representing the vibrations of aldehydic C–H, C=O, and aromatic C=C bonds, respectively (Fig. S3, ESI†); the spectrum of BCTA-4NH_2 featured three sharp adsorption bands at 3437, 3366, and 3209 cm^{-1} representing asymmetric and symmetric vibrations of N–H bonds, as well as a band at 1618 cm^{-1} representing aromatic C=C vibrations (Fig. S4, ESI†). The ^{1}H NMR spectrum of BCTB-4CHO featured a singlet at 10.06 ppm representing the four aldehydic CHO groups, in addition to signals for the aromatic CH groups in the range from 9.06 to 6.92 ppm (Fig. S9, ESI†); the spectrum of BCTA-4NH_2 featured a singlet at 5.18 ppm for the four amino NH_2 groups, in addition to signals for the aromatic CH groups in the range of 8.63–6.70 ppm (Fig. S11, ESI†). The ^{13}C NMR spectrum of BCTB-4CHO featured a signal at 193.80 ppm for the aldehydic CHO carbon nuclei (Fig. S10, ESI†), while that of BCTA-4NH_2 featured a signal at 149.14 ppm for the carbon nuclei of the CNH_2 groups (Fig. S12, ESI†).

Scheme 1 displays our syntheses of the three COFs from the new precursors. We obtained the target BCTB–PD and BCTB–BCTA COFs through Schiff base condensations of BCTB-4CHO with PD and BCTA-4NH_2, respectively, and the target BCTA–TP COF through the condensation of BCTA-4NH_2 with TP; all of these reactions were performed under solvothermal conditions, using a co-solvent of *n*-butanol/*o*-dichlorobenzene (1 : 1, v/v) containing 6 M acetic acid (10 v%) at 120 °C for 72 h. The chemical compositions of the as-prepared COFs were confirmed using FTIR and solid state NMR spectroscopy. The characteristic vibration bands of the aldehydic CHO and amino NH units of the starting materials BCTB-4CHO, BCTA-4NH_2, PD, and TP were completely absent from the FTIR spectra of the BCTB–PD, BCTA–TP, and BCTB–BCTA COFs, implying that Schiff base condensations had occurred between the various building blocks. New adsorption bands appeared at 1620, 1621,

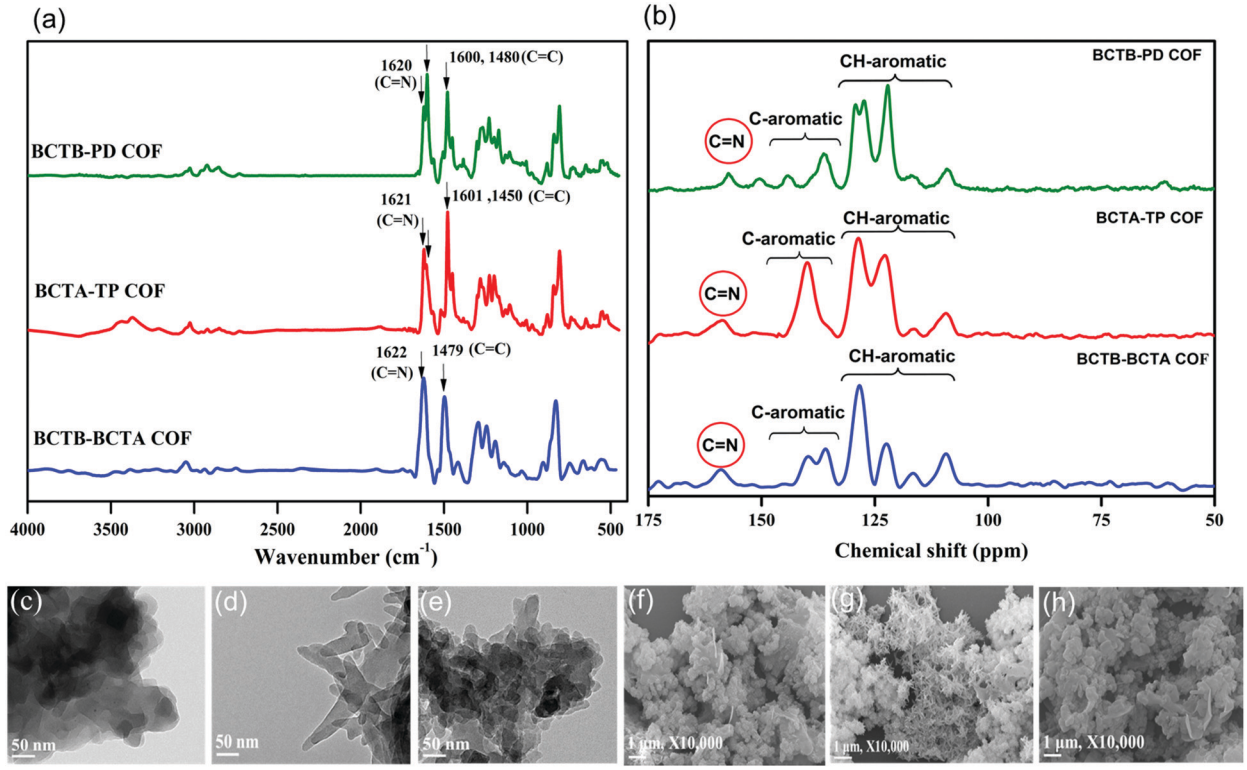

Fig. 1 (a) FTIR and (b) solid state ^{13}C CP/MAS NMR spectra of the BCTB–PD (olive), BCTA–TP (red), and BCTB–BCTA (blue) COFs; (c–e) TEM and (f–h) FE-SEM images of the (c and f) BCTB–PD, (d and g) BCTA–TP and (e and h) BCTB–BCTA COFs.

and 1622 cm^{-1} in the FTIR spectra of the BCTB–PD, BCTA–TP, and BCTB–BCTA COFs, respectively, representing their imino C═N vibrations (Fig. 1a and Fig. S13–S15, ESI†). The solid state ^{13}C NMR spectra of the BCTB–PD, BCTA–TP, and BCTB–BCTA COFs featured signals at 157.38, 158.67, and 159.13 ppm, respectively, for their C═N groups (Fig. 1b and Fig. S16–S18, ESI†). Each of these synthesized COFs exhibited excellent thermal stability, as determined through thermogravimetric analysis (TGA) under a N_2 atmosphere. Fig. S19 and Table S1 (ESI†) reveal that BCTB–PD and BCTB–BCTA were the most stable of our three COFs, with high decomposition temperatures (T_{d10}) of 566 and 522 °C, and char yields of 72 and 71 wt%, respectively; in contrast, the value of T_{d10} of the BCTA–TP COF was 402 °C and its char yield was 48 wt%. Thus, the use of BCTB-4CHO as the aldehydic building linker greatly enhanced the COFs, when compared with the effect of the other aldehydic TP building linker. Transmission electron microscopy (TEM) and field-emission scanning electron microscopy (FESEM) revealed the morphologies of the as-prepared COFs. The structures of the BCTB–PD, BCTA–TP, and BCTB–BCTA COFs featured porous networks (Fig. 1c–e and Fig. S20–S22, ESI†). The FESEM images of the BCTB–PD and BCTB–BCTA COFs revealed regularly distributed and loose aggregates, respectively, while the BCTA–TP COF displayed small stripe-like crystallites having lengths of approximately hundreds of nanometers and widths of tens of nanometers (Fig. 1f–h and Fig. S23, ESI†).

We used powder X-ray diffraction (PXRD) to examine the crystallinities of these new COFs. The BCTB–PD, BCTA–TP, and BCTB–BCTA COFs possessed excellent crystallinities, as evidenced by the appearance of strong sharp peaks at the 2θ values of 3.23, 3.42, and 4.47°, respectively, in their PXRD patterns (Fig. 2a–c and Fig. S24–S26, ESI†), representing their reflection (110) facets. Furthermore, the pattern of the BCTB–PD COF featured a set of other peaks at the 2θ values of 6.91 and 10.35°, attributed to the reflection (210) and (310) facets, respectively; these signals appeared, respectively, at 6.92 and 10.44° for the BCTA–TP COF and at 9.14 and 13.84° for the BCTB–BCTA COF. The last minor signals for the BCTB–PD, BCTA–TP, and BCTB–BCTA COFs appeared at 2θ values of 21.89, 21.92, and 21.25°, respectively, corresponding to their reflection (001) facets. From these PXRD patterns, we used the Bragg equation to calculate the d-spacings between the 110 planes of the COFs (d_{110}) and the π-stacking distances between their stacked interlayers. The d_{110} values for the BCTB–PD, BCTA–TP, and BCTB–BCTA COFs were 2.73, 2.58, and 1.97 nm, respectively, with the π-stacking distances of 3.99, 4.05, and 4.18 Å, respectively (Table S2, ESI†). To assess the crystalline framework structures of the BCTB–PD, BCTA–TP, and BCTB–BCTA COFs, we used the Material Studio software to model credible 2D layered structures featuring A–A eclipsed and A–B staggered stacking.[65] As revealed in Fig. 2a–c and Fig. S24–S26 (ESI†), the experimental PXRD patterns (Fig. 2a–c, black curves) of the BCTB–PD, BCTA–TP, and BCTB–BCTA COFs were more consistent with the simulated PXRD patterns for the A–A models (Fig. 2a–c, magenta curves), while they deviated from those of the A–B models (Fig. 2a–c, olive curves), suggesting the π-eclipsed stacking of the layers in our new COFs. Moreover, we subjected

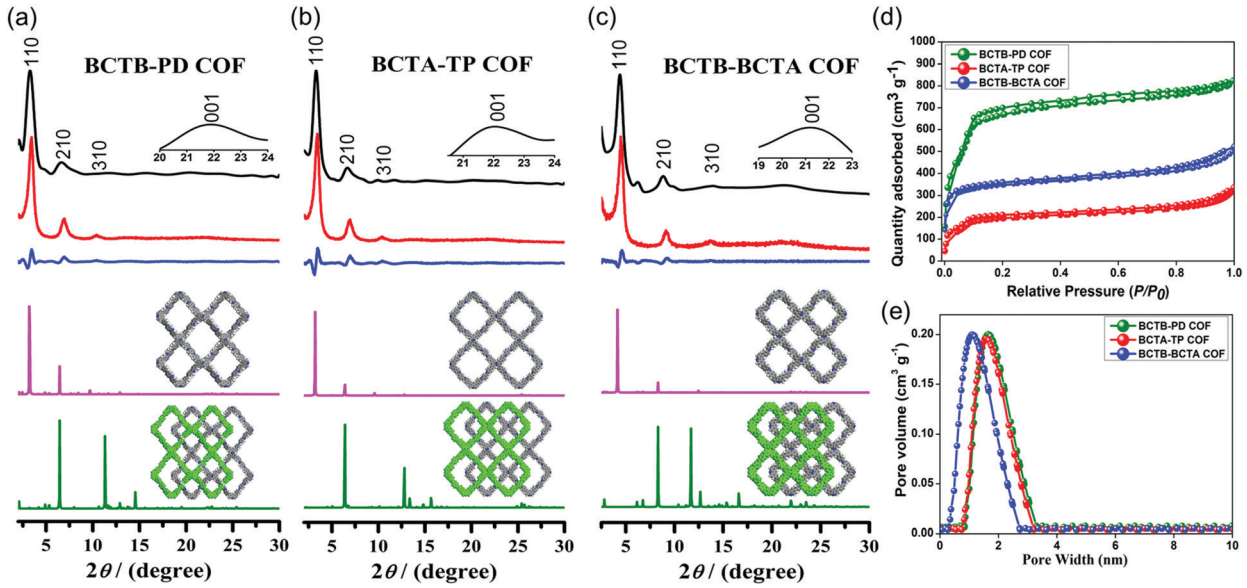

Fig. 2 (a–c) PXRD patterns of the (a) BCTB–PD, (b) BCTA–TP and (c) BCTB–BCTA COFs: experimental patterns (black), simulated Pawley refined patterns (red), their difference (blue), and simulated patterns obtained from the A–A (purple) and A–B (olive) stacking models; (d) N_2 sorption isotherms recorded at 77 K and (e) pore size distributions of the BCTB–PD (olive), BCTA–TP (red), and BCTB–BCTA (blue) COFs.

these A–A eclipsed packing models to subsequent Pawley refinement to produce theoretical PXRD patterns (Fig. 2a–c, red curves) that were consistent with the experimental ones (Fig. 2a–c, black curves), with only slight differences (Fig. 2a–c, blue curves). The refinement of the A–A eclipsed models provided the following unit cell parameters: for the BCTB–PD COF, a = 36.10 Å, b = 42.11 Å, c = 4.07 Å, and $\alpha = \beta = \gamma = 90^\circ$; for the BCTA–TP COF, $a = b$ = 16.22 Å, c = 3.57 Å, and $\alpha = \beta = \gamma = 90^\circ$; for the BCTB–BCTA COF, a = 28.80 Å, b = 31.63 Å, c = 4.04 Å, and $\alpha = \beta = \gamma = 90^\circ$ (Fig. S27–S32, Tables S3–S8, ESI†).

Nitrogen adsorption/desorption analyses revealed the permanent porosity properties of the as-prepared COFs (Fig. 2d). Initially, the COFs were activated by degassing under vacuum at 100 °C for 20 h. All of the activated COFs provided classical type I isotherms at 77 K, suggesting that they were microporous materials. According to the Brunauer–Emmett–Teller (BET) model, the BCTB–PD COF featured the highest BET surface area of 2212 $m^2\ g^{-1}$, with the BCTA–TP and BCTB–BCTA COFs having surface areas of 645 and 1098 $m^2\ g^{-1}$, respectively (Table S2, ESI†). We used the nonlocal density functional theory (NLDFT) to estimate the pore size distributions of the BCTB–PD, BCTA–TP, and BCTB–BCTA COFs, providing micropore sizes of 1.62, 1.55, and 1.10 nm, and pore volumes of 0.28, 0.31, and 0.35 $cm^3\ g^{-1}$, respectively (Fig. 2e and Table S2, ESI†). The significantly higher BET surface area of the BCTB–PD COF over the BCTA–TP COF could be attributed to the morphology difference of the BCTB–PD COF compared to the BCTA–TP COF (Fig. 1c–h and Fig. S23, ESI†). The PXRD patterns our COFs showed nonalteration of the positions and intensities of the peaks after nitrogen adsorption/desorption analyses (Fig. S24–S26, dark yellow curves, ESI†).

Because several carbazole-based materials have prominent photoluminescence properties,[1–3] we examined the photophysical properties of the precursors BCTB-4CHO and BCTA-4NH_2 by measuring their UV-vis absorption and fluorescence emission spectra in various solvents. Both BCTB-4CHO and BCTA-4NH_2 are highly soluble in various high- and low-polarity solvents, including tetrahydrofuran (THF), MeOH, dichloromethane (DCM), acetone, and dimethylformamide (DMF). As illustrated in Fig. S33 and S34 (ESI†), the UV-vis absorption maxima of BCTB-4CHO and BCTA-4NH_2 at a concentration of 10^{-4} M appeared in the regions 280–360 and 260–360 nm, respectively, representing the π–π^* transitions of the conjugated biscarbazolyl and phenyl moieties. Interestingly, these absorption maxima were affected strongly by the solvent; for BCTB-4CHO, they appeared at 310 nm in MeOH, 312 nm in THF, 314 nm in DCM, 316 nm in DMF, and 318 nm in acetone, while for BCTA-4NH_2 they appeared at 294 nm in MeOH, 296 nm in THF, 298 nm in DCM, 302 in DMF, and 314 nm in acetone. The blue-shifting of the absorption maxima in MeOH presumably arose from hydrogen bonding between the CHO groups in BCTB-4CHO and the NH_2 groups in BCTA-4NH_2 with the solvent, stabilizing the BCTB-4CHO and BCTA-4NH_2 precursors in their ground states.[66] On the other hand, the red-shifting of the absorption maxima in acetone presumably arose from the π-stacking of BCTB-4CHO or BCTA-4NH_2.[67]

We investigated the fluorescence properties of BCTB-4CHO and BCTA-4NH_2 at a concentration of 10^{-4} M in solvents of various polarities (Fig. S35a–f and S36a–f, ESI†). The fluorescence emission maxima of BCTB-4CHO in THF, MeOH, DCM, acetone, and DMF appeared at 449, 464, 448, 451, and 466 nm, respectively; for BCTA-4NH_2, they appeared at 429, 484, 423, 446, and 486 nm, respectively. Thus, the fluorescence emission wavelengths of BCTB-4CHO and BCTA-4NH_2 were strongly affected by the polarity of the solvent, with an increase in solvent polarity causing an increase in the fluorescence emission wavelength, that is, a solvatochromism effect.[68] We attribute this

solvatochromism (red-shifting) of the fluorescence emission in polar solvents to the hydrogen bonding of MeOH (OH) and acetone and DMF (C═O) with the CHO groups of BCTB-4CHO and the NH_2 groups of BCTA-4NH_2, thereby stabilizing the polar excited states of BCTB-4CHO and BCTA-4NH_2 and accelerating their intramolecular charge-transfer processes (solvent relaxation phenomenon).[69] The fluorescence images of BCTB-4CHO and BCTA-4NH_2 in various solvents revealed that both precursors exhibited blue emissions (Fig. S35g and S36g, ESI†).

Fluorescent materials having highly conjugated aromatic systems typically exhibit strong fluorescence emissions only in diluted solutions; conversely, their fluorescence emissions are generally quenched in the solid state or in solution at high concentrations, a phenomenon known as aggregation-caused quenching (ACQ),[70] which arises from strong face-to-face non-covalent interactions (π-stacking). Consequently, we investigated the effect of the concentration on the fluorescence emissions of BCTB-4CHO and BCTA-4NH_2 in THF, MeOH, DCM, acetone, and DMF. As revealed in Fig. S35a–f and S36a–f (ESI†), the emission intensities decreased upon increasing the concentration of BCTB-4CHO and BCTA-4NH_2 in each of these solvents, confirming their ACQ behavior. According to the excellent fluorescence properties of the precursors BCTB-4CHO and BCTA-4NH_2, we studied the photoluminescence behavior of our BCTB–PD, BCTA–TP, and BCTB–BCTA COFs by measuring their fluorescence emissions when dispersed as crystallites in various solvents. Typically, we prepared dispersions of the COF crystallites in the various solvents at a concentration of 1 mg mL^{-1}. Interestingly, excitation of the suspensions of the BCTB–PD and BCTB–BCTA COF crystallites in high polarity solvents, namely, pyridine, acetone, *N*-methyl-2-pyrrolidone (NMP), and DMF, with light from an ultraviolet lamp at a wavelength of 365 nm resulted in strong fluorescence, either blue green or light blue, that was visible to the naked eye, while the suspensions of the BCTB–PD and BCTB–BCTA COFs in dioxane and ethyl acetate (EA) showed moderate-to-weak pale violet fluorescence. In contrast, the suspensions of the BCTA–TP COF in the same solvents exhibited weak, almost dark, fluorescence colors (Fig. 3a–c). All the synthesized COFs showed very weak fluorescence emissions in THF. Moreover, we recorded the fluorescence emission spectra of these COF suspension solutions. Under 365 nm light, the suspensions of the BCTB–PD COF in pyridine, acetone, DMF, and NMP provided strong fluorescence emission maxima near 462, 469, 471, and 474 nm, while those in dioxane and EA provided moderate-to-weak fluorescence at 423 and 440 nm, respectively (Fig. 3d) (Table S9, ESI†). The suspensions of the BCTA–TP COF in dioxane, EA, pyridine, acetone, DMF, and NMP exhibited the weakest fluorescence emissions, with maxima near 399, 402, 420, 422, 430, and 443 nm, respectively (Fig. 3e) (Table S9, ESI†). Among our three COFs, the BCTB–BCTA COF exhibited the strongest

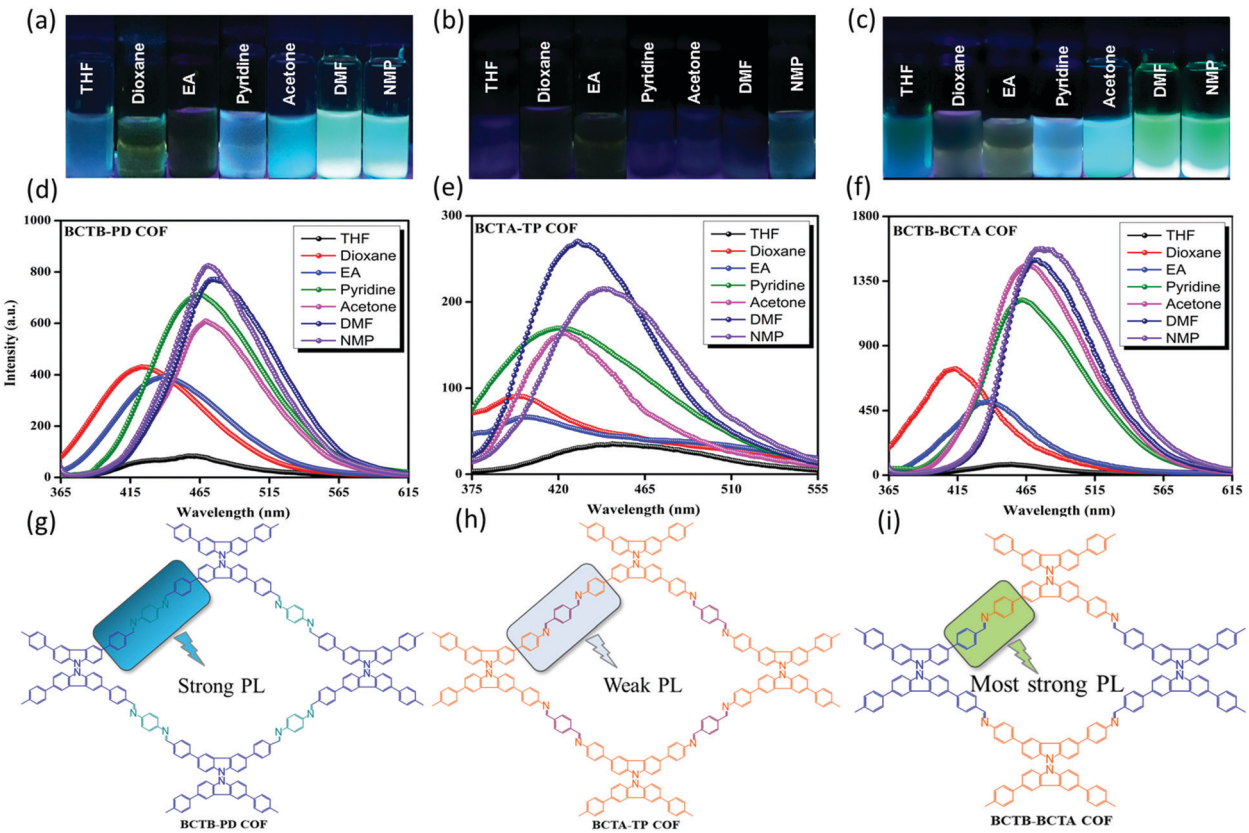

Fig. 3 (a–c) Photographic images of the (a) BCTB–PD, (b) BCTA–TP, and (c) BCTB–BCTA COFs dispersed in DMF (1 mg mL^{-1}) under excitation at 365 nm; (d–f) fluorescence spectra of the (d) BCTB–PD, (e) BCTA–TP and (f) BCTB–BCTA COFs dispersed in various solvents (1 mg mL^{-1}) under excitation at 365 nm; (g–i) fluorescence emission maxima of the (g) BCTB–PD, (h) BCTA–TP, and (i) BCTB–BCTA COFs.

fluorescence emissions in pyridine, acetone, DMF, and NMP with maxima near 461, 465, 472, and 476 nm, while that in dioxane and EA exhibited moderate-to-weak fluorescence at 411 and 437 nm, respectively (Fig. 3f) (Table S9, ESI†). This red-shifting of the fluorescence emission upon increasing the polarity of the solvent indicated that noncovalent interactions (*e.g.*, hydrogen bonding, dipole effects) between the COFs and the polar solvent molecules enhanced the stability of the excited states of the COFs and thus enhanced the excited-state intramolecular charge transfer (ICT).[71,72] All of the COF crystallites dispersed in THF displayed very weak fluorescence emissions, resulting from the lower polarity of THF. Thus, our as-prepared COFs emitted strong or very strong fluorescence only in solvents of moderate to high polarity. To support these observations, we recorded the absolute photoluminescence quantum yield (PLQY) values of our BCTB–PD, BCTA–TP, and BCTB–BCTA COFs as crystallites in various solvents. Table S9 (ESI†) summarizes the PLQY values of our COFs which indicate that the BCTB–PD COF provided strong fluorescence with PLQY values of 12.8, 13.5, 15.9, and 16.3% in pyridine, acetone, DMF, and NMP, respectively, and moderate fluorescence with PLQY values of 9.9 and 9.6% in dioxane and EA, respectively; for the BCTA–TP COF, these values were the lowest, which were 1.1, 0.9, 3.1, 3.8, 5.1, and 5.6% in pyridine, acetone, DMF, and NMP, respectively. The BCTB–BCTA COF showed the highest PLQY values of 17.6, 19.3, 20.8, and 21.2% in dioxane, EA, pyridine, acetone, DMF, and NMP, respectively, in addition to the moderate values of 13.8 and 12.5% in dioxane and EA, respectively. The PLQY values of the three COFs in THF were very weak (<1%). These findings suggest that the use of BCTB-4CHO as the linker for Schiff base condensation produced BCTB-4CH═N units that were significant electron-donating groups and provided a COF (BCTB–PD) capable of displaying strong fluorescence emission; in contrast, BCTA-4NH_2 produced BCTA-4N═CH units that were weak electron-donating groups and provided a COF (BCTA–TP) displaying weak fluorescence emission. In addition, the use of BCTB-4CHO, instead of TP, as the aldehydic linker in the Schiff base condensation produced a strongly fluorescent COF (BCTB–BCTA), confirming the importance of BCTB-4CHO as a linker. The highest fluorescence emission intensities among our three COFs were those of the BCTB–PD and BCTB–BCTA COFs, presumably due to significant ICT from the electron-donating carbazole BCTB-4CH═N units, which acted as donors to the phenyl or BCTA moieties acting as acceptors; within the BCTA–TP COF, however, ICT from the BCTA-4N═CH units to the phenyl groups was weak (Fig. 3g–i). In addition, the fluorescence emission intensity of the BCTB–BCTA COF was stronger than that of the BCTB–PD COF due to the greater π-stacking and crystallinity in the structure of the latter (π-stacking distances: 4.05 Å in the BCTB–PD COF and 4.18 Å in the BCTB–BCTA COF) (Table S2, ESI†). Thus, the type of Schiff base (BCTB-4CH═N or BCTA-4N═CH) and the strength of π-stacking between the COF layers both had major effects on the fluorescence behavior of the COFs. Furthermore, the chemical stability and crystallinity of the BCTB–PD, BCTA–TP, and BCTB–BCTA COFs in the solvents were investigated by immersing 50 mg of each COF in THF, dioxane, EA, pyridine, acetone, DMF, and NMP for 3 days, then isolating them using vacuum filtration and finally drying them at 120 °C overnight under vacuum. As shown in Fig. S37–S42 (ESI†), retention of the FTIR and PXRD peaks with a non-significant change after immersion in the solvents revealed the outstanding chemical stability and crystallinity of the COFs in these solvents.

Taking advantage of its strong fluorescence emission, we used the BCTB–BCTA COF as a sensitive and efficient fluorescence sensor for the detection of HCl. First, we investigated the influence of the concentration of HCl on the sensitivity of the fluorescence of the BCTB–BCTA COF by measuring its fluorescence spectra in DMF (1 mg mL^{-1}) in the presence of various amounts of HCl. Fig. 4a reveals that the addition of a trace amount of HCl (1 mmol L^{-1}) induced a considerable change in the fluorescence spectrum of the BCTB–BCTA COF; the fluorescence emission peak having its maximum at 472 nm disappeared completely, while a new peak appeared with its maximum at 495 nm (PLQY = 23.8%). This new fluorescence peak decreased in intensity upon increasing the concentration of HCl in the range from 1 to 25 mmol L^{-1}, but it remained approximately unchanged when increasing the concentration of HCl thereafter to 50 and 100 mmol L^{-1}. The relationship between the fluorescence emission intensity of the peak at 495 nm and the HCl concentration was linear in the range of 1–25 mmol L^{-1}; it was described using the equation: $I = 1648.56 - 48.89C$, where I is the fluorescence emission intensity and C is the concentration of HCl (mmol L^{-1}), with a correlation coefficient (R^2) of 0.989. The limit of detection (LOD) was calculated to be 10 nmol L^{-1} (Fig. 4b), according to the equation: LOD = $3S/b$, where b is the slope of the calibration curve and S is the standard deviation of the fluorescence response.

Next, we investigated the naked-eye detection of HCl gas by exposing a suspension of the BCTB–BCTA COF in DMF (1 mg L^{-1}) to HCl vapor under light at a wavelength of 365 nm. As revealed in Fig. 4c, upon exposure to HCl vapor, the fluorescence emission color of the COF suspension was changed from blue green to green within a response time of approximately 1 s. Upon subsequent exposure to NH_3 vapor, the green color emitted by the BCTB–BCTA COF returned to its original color of blue green. No degradation in fluorescence occurred upon alternating the exposure of the BCTB–BCTA COF to HCl and NH_3 vapors for up to 10 cycles, confirming its excellent reproducibility when used as an HCl sensor. In addition, the crystallinity of the BCTB–BCTA COF after recycling 10 times was examined as shown in Fig. S43 (ESI†), which reveals the nonalteration of peaks in the PXRD pattern, thus promoting the utilization of the BCTB–BCTA COF as an HCl sensor. Fig. 4d provides a schematic representation of the mechanism of HCl sensing when using our BCTB–BCTA COF. At an HCl concentration of 1 mmol L^{-1}, protonation of the imino nitrogen atoms in the COF architecture might have occurred, thus increasing the planarity of the units in the BCTB–BCTA COF and, hence, expanding its conjugated system, which resulted in a red-shift in the fluorescence emission.[73,74] At higher HCl concentrations,

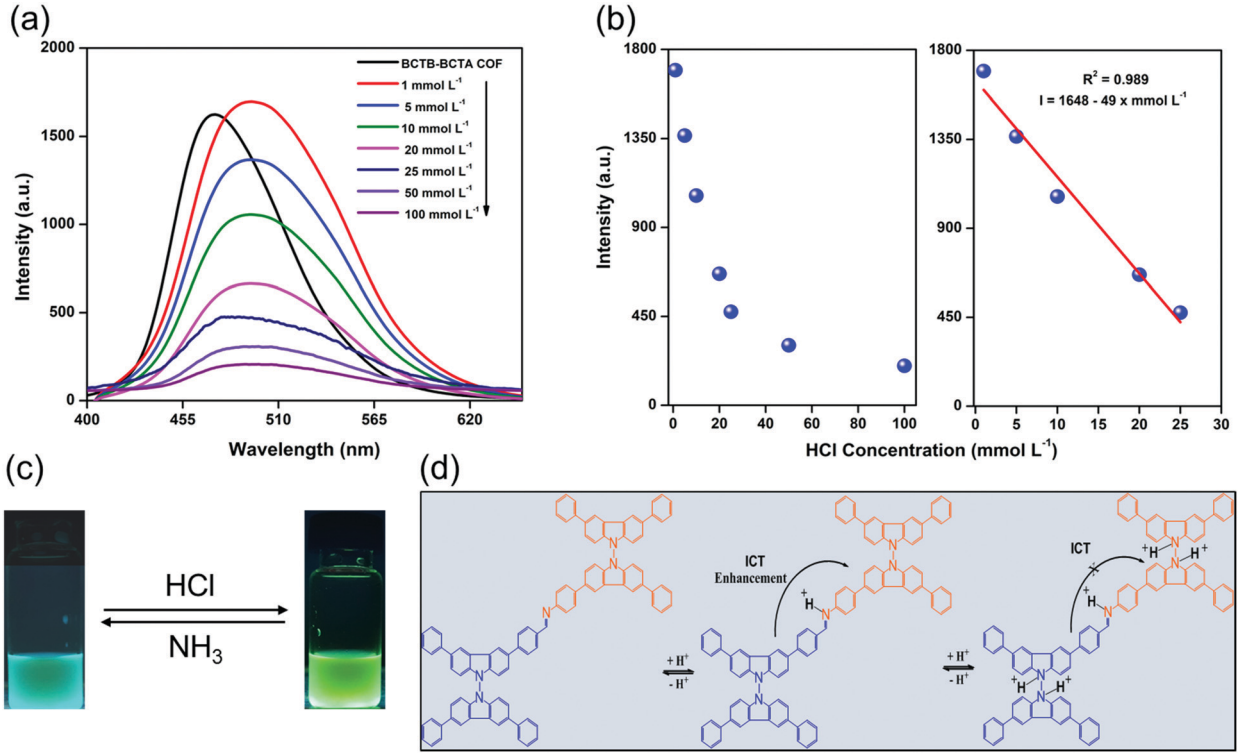

Fig. 4 (a) Fluorescence spectra of the BCTB–BCTA COF dispersed in DMF (1 mg mL^{-1}) under excitation at 365 nm in the presence of various amounts of HCl; (b) photographs of the BCTB–BCTA COF dispersed in DMF (1 mg mL^{-1}) under excitation at 365 nm after the exposure to HCl and then NH_3 vapor; (c) calibration curve of the fluorescence intensity of the BCTB–BCTA COF plotted with respect to the concentration of HCl; (d) mechanism of the protonation and deprotonation of the BCTB–BCTA COF.

protonation of the other nitrogen atoms in the COF architecture would also occur, interfering with the ICT of the BCTB–BCTA COF.

The protonation of imine bonds in the skeleton of the BCTB–BCTA COF was confirmed by recording the FTIR spectrum of the BCTB–BCTA COF after treatment with 1 mmol L^{-1} HCl concentration (known as BCTB–BCTA COF–HCl). As shown in Fig. S44 (ESI†), the appearance of a new peak at 1595 cm^{-1} could be observed in the BCTB–BCTA COF–HCl spectrum, which is attributed to the C═NH$^+$ stretching vibration, accompanied by an alleviation of the stretching vibration of the imine (C═N) peak, consistent with the previous study.[75,76] As a result, the imine nitrogen atoms in the skeleton of the BCTB–BCTA COF underwent rapid protonation in the presence of HCl (1 mmol L^{-1}), which affected the conjugate structure of the skeleton of the BCTB–BCTA COF and thus caused the red-shifting in the fluorescence emission and color of the COF.[73,74] In addition, it has been reported that protonated imine groups (C═NH$^+$) are stronger electron acceptors than their free imine (C═N) groups, thus increasing the charge transfer process and decreasing the transition energies.[76] Similarly, the C═NH$^+$ groups in the skeleton of BCTB–BCTA COF–HCl would have increased the charge transfer process from the electron-donating carbazole units to the BCTA moieties and decreased their transition energies, thus leading to this red-shifting. Furthermore, these concepts were supported by measuring the fluorescence life-time decays of the BCTB–BCTA COF and BCTB–BCTA COF–HCl. The fluorescence life-time of the BCTB–BCTA COF was 4.13 ns, while after the addition of 1 mmol L^{-1} HCl (BCTB–BCTA COF–HCl) it was 4.89 which further confirmed the red-shift in the fluorescence emission of the BCTB–BCTA COF upon the addition of HCl (Fig. S45, ESI†). Our findings suggest that the BCTB–BCTA COF is a promising fluorescence chemosensor for the sensitive and rapid spectroscopic detection of HCl in organic solvents.

Conclusions

We have synthesized three stable luminescent COFs, namely, BCTB–PD, BCTA–TP, and BCTB–BCTA, through [4+2] and [4+4] polycondensations of BCTB-4CHO with PD, of BCTA-4NH$_2$ with TP, and of BCTB-4CHO with BCTA-4NH$_2$, respectively. The FTIR and solid state ^{13}C NMR spectra confirmed the chemical compositions of these new COFs. The PXRD and thermal analyses of these COFs revealed their excellent crystallinity and high thermal stability (as high as 566 °C); furthermore, they had BET surface areas as high as 2212 m^2 g^{-1}. More interestingly, the type of Schiff bases (BCTB-4CH═N or BCTA-4N═CH) and the strength of π-stacking between the COF layers influenced the ICT from the donor units to the acceptors, thereby also impacting the fluorescence of the resultant COFs. For example, the BCTB–BCTA COF, which featured BCTB-4CH═N Schiff base linkages and the longest π-stacking distance (4.18 Å), exhibited the strongest fluorescence, whereas the BCTA–TP COF, which featured BCTA-4N═CH Schiff base

linkages and a shorter π-stacking distance (4.05 Å), exhibited very weak fluorescence. Due to displaying the strongest fluorescence emission, the BCTB–BCTA COF was most suitable for HCl sensing. This COF displayed a highly sensitive (up to 10 nmol L^{-1}) and rapid response toward the spectroscopic detection of HCl in solution. Consequently, this paper describes a new strategy for the construction of potentially luminescent COFs for use as responsive sensing platforms.

Conflicts of interest

There are no conflicts to declare.

Acknowledgements

This study was supported financially by the Ministry of Science and Technology, Taiwan, under contracts MOST 106-2221-E-110-067-MY3, 108-2638-E-002-003-MY2, 108-2218-E-110-013-MY3, and 108-2221-E-110-014-MY3. We also thank Mr Hsien-Tsan Lin of the Regional Instruments Center at National Sun Yat-Sen University for his help with the TEM measurements.

Notes and references

1 B. Wex and B. R. Kaafarani, *J. Mater. Chem. C*, 2017, **5**, 8622–8653.
2 M. Meier, L. Ji, J. Nitsch, I. Krummenacher, A. Deißenberger, D. Auerhammer, M. Schäfer, T. B. Marder and H. Braunschweig, *Chem. – Eur. J.*, 2019, **25**, 4707–4712.
3 T. Nishimoto, T. Yasuda, S. Y. Lee, R. Kondo and C. Adachi, *Mater. Horiz.*, 2014, **1**, 264–269.
4 A. F. M. El-Mahdy, C. Young, J. Kim, J. You, Y. Yamauchi and S. W. Kuo, *ACS Appl. Mater. Interfaces*, 2019, **11**, 9343–9354.
5 A. F. M. EL-Mahdy, Y.-H. Hung, T. H. Mansoure, H. H. Yu, Y. S. Hsu, K. C. Wu and S. W. Kuo, *J. Taiwan Inst. Chem. Eng.*, 2019, **103**, 199–208.
6 C. W. Huang, W. Y. Ji and S. W. Kuo, *Polym. Chem.*, 2018, **9**, 2813–2820.
7 C. W. Huang, W. Y. Ji and S. W. Kuo, *Macromolecules*, 2017, **50**, 7091–7101.
8 B. H. Mao, A. F. M. EL-Mahdy and S. W. Kuo, *J. Polym. Res.*, 2019, **26**, 208.
9 C. W. Huang, F. C. Chang, Y. L. Chu, C. C. Lai, T. E. Lin, C. Y. Zhu and S. W. Kuo, *J. Mater. Chem. C*, 2015, **3**, 8142–8151.
10 H. K. Shih, Y. H. Chen, Y. L. Chu, C. C. Cheng, F. C. Chang, C. Y. Zhu and S. W. Kuo, *Polymers*, 2015, **7**, 804–818.
11 Y. Ma, Y. Tang, Y. Zhao and W. Lin, *Anal. Chem.*, 2019, **91**, 10723–10730.
12 Y. Feng, D. Li, Q. Wang, S. Wang, X. Meng, Z. Shao, M. Zhu and X. Wang, *Sens. Actuators, B*, 2016, **225**, 572–578.
13 D. Li, Y. Feng, J. Lin, M. Chen, S. Wang, X. Wang, H. Sheng, Z. Shao, M. Zhu and X. Meng, *Sens. Actuators, B*, 2016, **222**, 483–491.
14 Y. Liu, J. Niu, W. Wang, Y. Ma and W. Lin, *Adv. Sci.*, 2018, **5**, 1700966.
15 F. Gao, L. Li, J. Fan, J. Cao, Y. Li, L. Chen and X. Peng, *Anal. Chem.*, 2019, **91**, 3336–3341.
16 P. Ning, L. Hou, Y. Feng, G. Xu, Y. Bai, H. Yu and X. Meng, *Chem. Commun.*, 2019, **55**, 1782–1785.
17 M. Peng, J. Yin and W. Lin, *Spectrochim. Acta, Part A*, 2019, **224**, 117310.
18 J. Yin, M. Peng and W. Lin, *Sens. Actuators, B*, 2019, **288**, 251–258.
19 Y. Kim, C. E. Song, S.-J. Moon and E. Lim, *Chem. Commun.*, 2014, **50**, 8235–8238.
20 K. Wang, Y. Firdaus, M. Babics, F. Cruciani, Q. Saleem, A. El Labban, M. A. Alamoudi, T. Marszalek, W. Pisula, F. Laquai and P. M. Beaujuge, *Chem. Mater.*, 2016, **28**, 2200–2208.
21 A. M. Raynor, A. Gupta, H. Patil, D. Ma, A. Bilic, T. J. Rook and S. V. Bhosale, *RSC Adv.*, 2016, **6**, 28103–28109.
22 P. J. Waller, F. Ga'ndara and O. M. Yaghi, *Acc. Chem. Res.*, 2015, **48**, 3053.
23 M. S. Lohse and T. Bein, *Adv. Funct. Mater.*, 2018, **28**, 1705551.
24 S. Wang, L. Ma, Q. Wang, P. Shao, D. Ma, S. Yuan, P. Lei, P. Li, X. Feng and B. Wang, *J. Mater. Chem. C*, 2018, **6**, 5369–5374.
25 A. F. M. EL-Mahdy, M. G. Mohamed, T. H. Mansoure, H. H. Yu, T. Chen and S.-W. Kuo, *Chem. Commun.*, 2019, **55**, 14890–14893.
26 K. E. Cordova and O. M. Yaghi, *Mater. Chem. Front.*, 2017, **1**, 1304.
27 A. F. M. El-Mahdy, C. H. Kuo, A. Alshehri, C. Young, Y. Yamauchi, J. Kim and S. W. Kuo, *J. Mater. Chem. A*, 2018, **6**, 19532–19541.
28 A. P. Côté, A. I. Benin, N. W. Ockwig, M. O'Keeffe, A. J. Matzger and O. M. Yaghi, *Science*, 2005, **310**, 1166–1170.
29 J. W. Colson and W. R. Dichtel, *Nat. Chem.*, 2013, **5**, 453–465.
30 S. Y. Ding and W. Wang, *Chem. Soc. Rev.*, 2013, **42**, 548–568.
31 H. R. Abuzeid, A. F. M. EL-Mahdy and S. W. Kuo, *Microporous Mesoporous Mater.*, 2020, **300**, 110151.
32 Y. Zeng, R. Zou and Y. Zhao, *Adv. Mater.*, 2016, **28**, 2855–2873.
33 L. A. Baldwin, J. W. Crowe, D. A. Pyles and P. L. McGrier, *J. Am. Chem. Soc.*, 2016, **138**, 15134–15137.
34 A. F. M. El-Mahdy, Y. H. Hung, T. H. Mansoure, H. H. Yu, T. Chen and S. W. Kuo, *Chem. – Asian J.*, 2019, **14**, 1429–1435.
35 S. Lin, C. S. Diercks, Y. B. Zhang, N. E. Kornienko, M. Nichols, Y. B. Zhao, A. R. Paris, D. Kim, P. Yang, O. M. Yaghi and C. J. Chang, *Science*, 2015, **349**, 1208–1213.
36 X. Yan, H. Liu, Y. Li, W. Chen, T. Zhang, Z. Zhao, G. Xing and L. Chen, *Macromolecules*, 2019, **52**, 7977–7983.
37 L. Bai, S. Z. F. Phua, W. Q. Lim, A. Jana, Z. Luo, H. P. Tham, L. Zhao, Q. Gao and Y. Zhao, *Chem. Commun.*, 2016, **52**, 4128–4131.
38 S. Chandra, T. Kundu, S. Kandambeth, R. BabaRao, Y. Marathe, S. M. Kunjir and R. Banerjee, *J. Am. Chem. Soc.*, 2014, **136**, 6570–6573.
39 H. Xu, S. Tao and D. Jiang, *Nat. Mater.*, 2016, **15**, 722–726.
40 P. Das and S. K. Mandal, *J. Mater. Chem. A*, 2018, **6**, 16246–16256.
41 Q. Gao, X. Li, G. H. Ning, K. Leng, B. Tian, C. Liu, W. Tang, H. S. Xu and K. P. Loh, *Chem. Commun.*, 2018, **54**, 2349–2352.
42 Z. Li, Y. Zhang, H. Xia, Y. Mu and X. Liu, *Chem. Commun.*, 2016, **52**, 6613–6616.

43 G. Lin, H. Ding, D. Yuan, B. Wang and C. Wang, *J. Am. Chem. Soc.*, 2016, **138**, 3302–3305.
44 M. G. Mohamed, A. F. M. EL-Mahdy, M. M. M. Ahmed and S. W. Kuo, *ChemPlusChem*, 2019, **84**, 1767–1774.
45 C. Gu, N. Hosono, J. J. Zheng, Y. Sato, S. Kusaka, S. Sakaki and S. Kitagawa, *Science*, 2019, **363**, 387–391.
46 F. Zhang, J. Zhang, B. Zhang, X. Tan, D. Shao, J. Shi, D. Tan, L. Liu, J. Feng and B. Han, *ChemSusChem*, 2018, **11**, 3576–3580.
47 P. Pachfule, A. Acharjya, J. R. M. Roeser, T. Langenhahn, M. Schwarze, R. Schomacker, A. Thomas and J. Schmidt, *J. Am. Chem. Soc.*, 2018, **140**, 1423–1427.
48 V. Nguyen and M. Grünwald, *J. Am. Chem. Soc.*, 2018, **140**, 3306–3311.
49 H. R. Abuzeid, A. F. M. EL-Mahdy, M. M. M. Ahmed and S. W. Kuo, *Polym. Chem.*, 2019, **10**, 6010–6020.
50 S. Kandambeth, A. Mallick, B. Lukose, M. V. Mane, T. Heine and R. Banerjee, *J. Am. Chem. Soc.*, 2012, **134**, 19524–19527.
51 S. Dalapati, S. Jin, J. Gao, Y. Xu, A. Nagai and D. Jiang, *J. Am. Chem. Soc.*, 2013, **135**, 17310–17313.
52 L. Wang, C. Zeng, H. Xu, P. Yin, D. Chen, J. Deng, M. Li, N. Zheng, C. Gu and Y. Ma, *Chem. Sci.*, 2019, **10**, 1023–1028.
53 Q. Gao, X. Li, G. H. Ning, K. Leng, B. Tian, C. Liu, W. Tang, H. S. Xu and K. P. Loh, *Chem. Commun.*, 2018, **54**, 2349–2352.
54 X. Li, Q. Gao, J. Wang, Y. Chen, Z. H. Chen, H. S. Xu, W. Tang, K. Leng, G. H. Ning, J. Wu, Q. H. Xu, S. Y. Quek, Y. Lu and K. P. Loh, *Nat. Commun.*, 2018, **9**, 2335.
55 L. Chen, L. He, F. Ma, W. Liu, Y. Wang, M. A. Silver, L. Chen, L. Zhu, D. Gui, J. Diwu, Z. Chai and S. Wang, *ACS Appl. Mater. Interfaces*, 2018, **10**, 15364–15368.
56 R. Xue, H. Guo, T. Wang, L. Gong, Y. Wang, J. Ai, D. Huang, H. Chen and W. Yang, *Anal. Methods*, 2017, **9**, 3737–3750.
57 S. Y. Ding, M. Dong, Y. W. Wang, Y. T. Chen, H. Z. Wang, C. Y. Su and W. Wang, *J. Am. Chem. Soc.*, 2016, **138**, 3031–3037.
58 S. Dalapati, S. Jin, J. Gao, Y. Xu, A. Nagai and D. Jiang, *J. Am. Chem. Soc.*, 2013, **135**, 17310–17313.
59 Y. F. Xie, S. Y. Ding, J. M. Liu, W. Wang and Q. Y. Zheng, *J. Mater. Chem. C*, 2015, **3**, 10066–10069.
60 G. Chen, H. H. Lan, S. L. Cai, B. Sun, X. L. Li, Z. H. He, S. R. Zheng, J. Fan, Y. Liu and W. G. Zhang, *ACS Appl. Mater. Interfaces*, 2019, **11**(13), 12830–12837.
61 S. L. Cai, Z. H. He, X. L. Li, K. Zhang, S. R. Zheng, J. Fan, Y. Liu and W. G. Zhang, *Chem. Commun.*, 2019, **55**, 13454–13457.
62 Z. Li, N. Huang, K. H. Lee, Y. Feng, S. Tao, Q. Jiang, Y. Nagao, S. Irle and D. Jiang, *J. Am. Chem. Soc.*, 2018, **140**(39), 12374–12377.
63 M. Li, Z. Cui, S. Pang, L. Meng, D. Ma, Y. Li, Z. Shi and S. Feng, *J. Mater. Chem. C*, 2019, **7**, 11919–11925.
64 F. Z. Cui, J. J. Xie, S. Y. Jiang, S. X. Gan, D. L. Ma, R. R. Liang, G. F. Jiang and X. Zhao, *Chem. Commun.*, 2019, **55**, 4550–4553.
65 Accelrys Software Inc., *Materials Studio 5.0: Modeling Simulation for Chemical and Material*, San Diego, CA, 2009.
66 A. F. M. EL-Mahdy and S. W. Kuo, *RSC Adv.*, 2018, **8**, 15266–15281.
67 A. F. M. EL-Mahdy and S. W. Kuo, *Polymer*, 2018, **156**, 10–21.
68 E. M. S. Castanheira and J. M. G. Martinho, *Chem. Phys. Lett.*, 1991, **185**, 319–323.
69 Y. Y. Lv, J. Wu and Z. K. Xu, *Sens. Actuators, B*, 2010, **148**, 233–239.
70 S. A. Jenekhe and J. A. Osaheni, *Science*, 1994, **265**, 765–768.
71 A. S. Klymchenko, *Acc. Chem. Res.*, 2017, **50**, 366–375.
72 K. Li, J. Cui, Z. Yang, Y. Huo, W. Duan, S. Gong and Z. Liu, *Dalton Trans.*, 2018, **47**, 15002–15008.
73 Y. Z. Xie, G. G. Shan, Z. Y. Zhou and Z. M. Su, *Sens. Actuators, B*, 2013, **177**, 41–49.
74 P. Muthukumar and S. A. John, *Sens. Actuators, B*, 2011, **159**, 238–244.
75 J. W. Ledbetter, *J. Phys. Chem.*, 1977, **81**, 54–59.
76 L. Ascherl, E. W. Evans, J. Gorman, S. Orsborne, D. Bessinger, T. Bein, R. H. Friend and F. Auras, *J. Am. Chem. Soc.*, 2019, **141**, 5693–15699.

